Applied Radiation and Isotopes 176 (2021) 109853

Contents lists available at ScienceDirect

Applied Radiation and Isotopes

journal homepage: www.elsevier.com/locate/apradiso

# Optimization of the electron beam dump for a GeV-class laser electron accelerator

T. Shi [a], D. Sun [a], I. Jovanovic [a,b,*], G. Kalinchenko [b,c], K. Krushelnick [a,b], C.C. Kuranz [a,b], A. Maksimchuk [b,c], J. Nees [b,c], A.G.R. Thomas [a,b], L. Willingale [b,c]

[a] Department of Nuclear Engineering and Radiological Sciences, University of Michigan, Ann Arbor, MI 48109, United States
[b] Gérard Mourou Center for Ultrafast Optical Science, University of Michigan, Ann Arbor, MI 48109, United States
[c] Department of Electrical Engineering and Computer Science, University of Michigan, Ann Arbor, MI 48109, United States

ARTICLE INFO

*Keywords:*
Radiation shielding
Electron accelerator
Monte Carlo simulation

ABSTRACT

The advances of laser-driven electron acceleration offer the promise of great reductions in the size of high-energy electron accelerator facilities. Accordingly, it is desirable to design compact radiation shielding for such facilities. A key component of radiation shielding is the high-energy electron beam dump. In an effort to optimize the electron beam dump design, different material combinations have been simulated with the FLUKA Monte Carlo code in the range of 1–40 GeV. The studied beam dump configurations consist of alternating layers of high-Z material (lead or iron) and low-Z material (high-density concrete or borated polyethylene) in either three-layer or five-layer structures. The designs of various beam dump configuration have been compared and it has been found that the iron and concrete stacking in a three-layer structure with a thick iron layer results in the lowest dose at 1, 10, and 40 GeV. The performance of the beam dump exhibits a strong dependence on the selected materials, the stacking method, the beam dump thickness, as well as the electron energy. This parametric study provides general insights that can be used for compact shielding design of future electron accelerator facilities.

## 1. Introduction

Electron accelerators based on laser–plasma interactions can produce ultrahigh accelerating gradient and greatly reduce their size and cost when compared to the conventional accelerator technology (Esarey et al., 2009). With the continuous development of the laser wakefield acceleration technique (Mangles et al., 2004; Geddes et al., 2004; Faure et al., 2004), the maximum electron energy has kept increasing (Maksimchuk et al., 2007, 2008; Leemans et al., 2014), and recently quasi-monoenergetic 7.8-GeV electrons have been produced (Gonsalves et al., 2019). For GeV-level accelerators, several meters of radiation shielding or a beam dump combined with radiation shielding are required to reduce the radiation dose to a safe level. With the laser plasma accelerator, it is now possible to condense the conventional kilometers-long accelerator facility to modest single building-size lab dimensions. Therefore, there is a commensurate need to develop compact shielding designs that can meet the overall size and cost objectives for laser-driven accelerator facilities. The optimization of the electron beam dump discussed in this work is motivated by those considerations as part of the shielding design for the Zettawatt-Equivalent Ultrashort pulse laser System (ZEUS) at the University of Michigan (Nees et al., 2020), where the overall design goal is to limit the hourly dose to 0.02 mSv/h (2 mrem/h) and the annual dose to 1 mSv/year (100 mrem/year), according to the radiation safety regulations.

Shielding of electron accelerators needs to take into account multiple aspects of accelerator performance and laboratory design. A comprehensive review of the radiation protection in high-energy electron accelerator facilities has been presented in Ref. Vylet and Liu (2001), where various source terms and analytical dose estimations are discussed. First, the facility bulk shielding along with the beam dump needs to ensure that the effective dose rate and the annual effective dose are below the regulatory limit. The dose rate limit is usually set to 2.5 μSv – 20 μSv depending on the combination of accelerator facility operational objectives and local regulation (OECD, 2015; Mao et al., 2011). The annual dose is usually controlled to be less than 1 mSv – 5 mSv (OECD, 2015; Englbrecht et al., 2020). Although the radiation induced by GeV-level electrons is forward peaked, the electron beam needs to be fully enclosed by the shielding including the roof to protect people from the so-called "skyshine" (Vylet and Liu, 2001). Neutrons and high-energy photons are major sources of secondary radiation, and production of muons also becomes significant when the electron energy

* Corresponding author at: Department of Nuclear Engineering and Radiological Sciences, University of Michigan, Ann Arbor, MI 48109, United States.
*E-mail address:* ijov@umich.edu (I. Jovanovic).

https://doi.org/10.1016/j.apradiso.2021.109853
Received 1 December 2020; Received in revised form 6 June 2021; Accepted 30 June 2021
Available online 9 July 2021

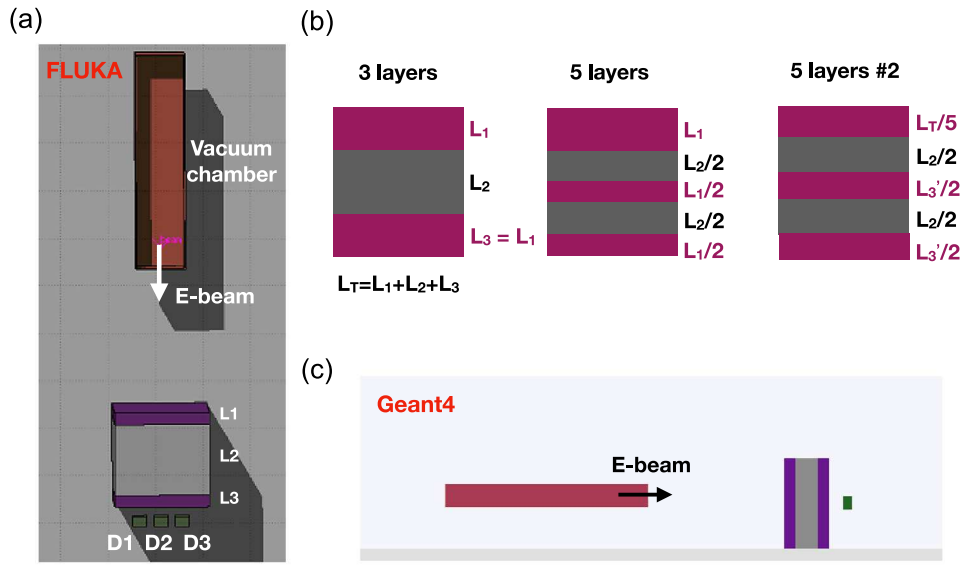


**Fig. 1.** (a) Simulation geometry (top view) in the Monte Carlo code FLUKA. (b) Different stacking methods are used to test the effectiveness of the radiation shielding. (c) The same simulation geometry (side view) is also defined in the Geant4 for comparison.

is higher than 1 GeV (Vylet and Liu, 2001; Rokni et al., 2007). In addition to the prompt radiation, the induced activity from activation of beamline components and surrounding materials (*e.g.,* shielding, walls, air, water) also needs to be assessed (Stevenson, 2001). A wide range of electron energies, beam power and target materials are used in accelerator experiments, which has great impact on the spatial dose distribution. Therefore, the shielding design needs to take into account a variety of experimental conditions to identify the most demanding shielding scenarios.

GeV electron beams are highly penetrating, and the bremsstrahlung and muon secondary production have a strong forward-directed component. The electron beam dump is an essential component of the overall radiation shielding design, which is why we choose to study its design and performance in detail. The front beam dump should not only reduce the dose in the forward direction, but also minimize the backscatter so that less shielding is needed in other directions. At the Stanford Linear Accelerator Center (SLAC), a combination of iron and concrete is used for the beam dump (Rokni et al., 2007; Rokni, 1996). At the Center for Advanced Laser Applications (CALA), magnetite concrete – a magnetite aggregate containing water and lead – is used for the beam dump and lab walls (Englbrecht et al., 2020). In the shielding studies from the Extreme Light Infrastructure (ELI), a three-material beam dump consisting of borated polyethylene, carbon fibers, and stainless steel has been shown to have good performance (Ferrari et al., 2013).

In this work, various material combinations with different thicknesses and stacking methods are simulated with the FLUKA Monte Carlo code (Battistoni et al., 2007). For an actual shielding design, the electron beam should be fully enclosed inside the radiation shielding. Here, we focus on the front beam dump because the exact design of the lateral and top shielding depends heavily on the detailed laboratory architecture, the thickness and materials constraints for the lab walls, the target, as well as the distance of the electron beam from the accessible areas. Instead of simulating a specific laboratory, the objective of this work is to understand the impact of different material combinations on electron beam shielding and to provide more general guidance that can be used in future accelerator facilities, particularly those based on laser wakefield acceleration.

This article is organized as follows: first, the simulation parameters are described. Next, different material combinations are studied at an electron energy of 10 GeV for various shielding thicknesses. Results from Geant4 and FLUKA simulations are also compared. Next, a comparison is drawn for the beam dump performance between a three-layer structure and a five-layer structure in which low-Z and high-Z materials are interleaved. At the end, the performance of different beam dump configurations is studied at 1 GeV and 40 GeV, and the dose results under different conditions are summarized.

## 2. Methods

In order to provide results that are applicable to various accelerator facilities, a simplified geometry has been simulated in the FLUKA code (version 2020.0.3), as shown in Fig. 1(a). The electron beam is 1 m above the concrete floor and is located inside a vacuum chamber consisting of 2.2 cm-thick iron. A 0.8-cm thick borosilicate viewport replaces the chamber wall along the exit path of the electron beam. The beam dump is placed 3 m away from the electron source. Simulations show that the energy loss in air is a small fraction of the initial electron energy and, thus, the distance between the source and the beam dump has little impact on the dose. For different beam dump configurations, an electron energy of 1 GeV, 10 GeV, and 40 GeV is used, and we assume that the electron beam has negligible divergence.

The beam dump is made of a combination of low-Z material and high-Z material stacked in an either three-layer or five-layer structure, as illustrated in Fig. 1(b). High-density (HD) concrete or 5 wt.% boron-loaded polyethylene are used as low-Z materials, while lead or iron are used as high-Z materials. We chose this low-Z/high-Z material combination because low-Z materials are effective in slowing down neutrons while high-Z materials are effective in attenuating and absorbing gammas and electrons. The high-Z material is sandwiched between layers of low-Z materials, which is motivated by the desire to reduce the energy and flux of secondary fast neutrons leaving the beam dump, since fast neutrons have a high damage effectiveness for human tissue. The five-layer stacking method is simulated with the goal to test the shielding effectiveness in the method where the neutrons, gammas, and electrons are gradually slowed down. For the three-layer design, we assume that the first and the last layer have the same thickness $L_1$. In this way, with the total shielding thickness fixed, only the thickness of the high-Z layer ($L_2$) is varied. For the five-layer design, similar assumptions are also made to reduce the number of thickness parameters. For the first five-layer design, as illustrated in the middle schematics of Fig. 1(b), the first layer has the same thickness ($L_1$) as that in the three-layer design. This will ensure a similar magnitude of

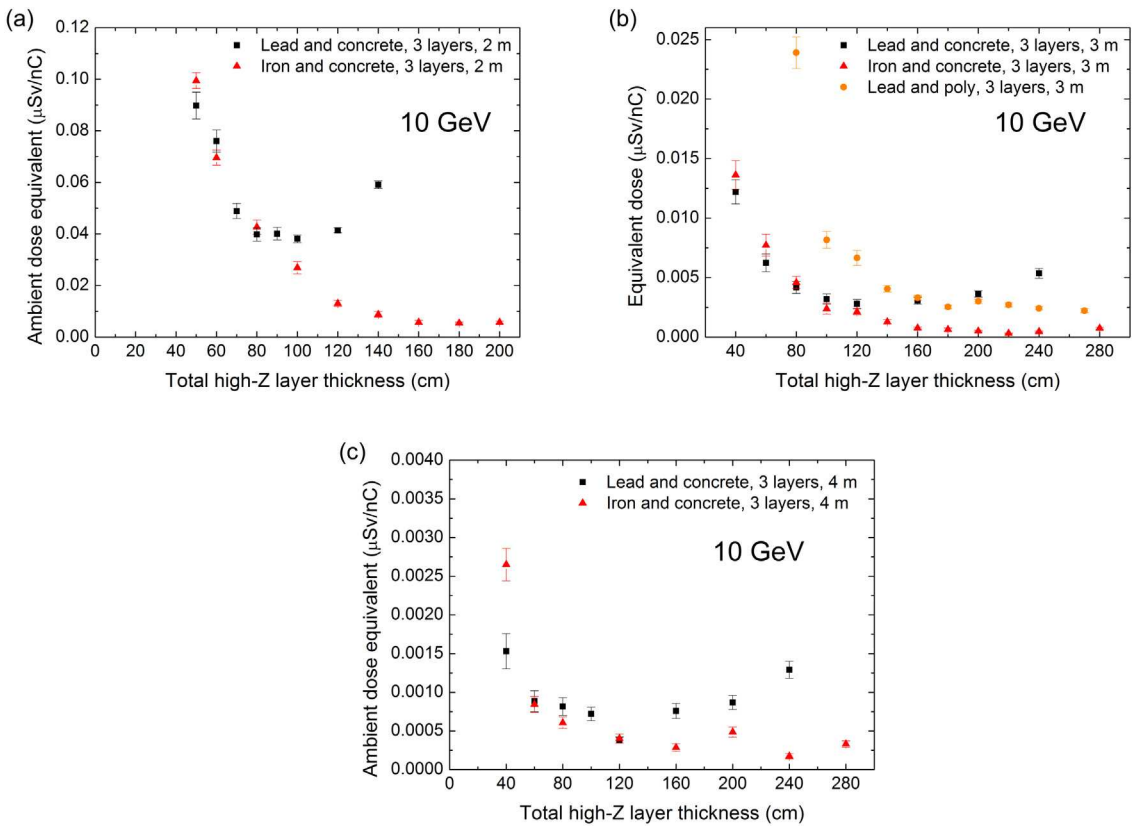


**Fig. 2.** Variation of the ambient dose equivalent with the high-Z layer thickness for different shielding configurations for an electron energy of 10 GeV with a total shielding thickness of (a) 2 m, (b) 3 m, and (c) 4 m. The shielding stack consists of one layer of high-Z material (lead or iron) sandwiched by two layers of low-Z material (HD concrete or 5 wt.% boron-loaded polyethylene). For a total thickness of 2 m, 3 m, and 4 m, on average $1.5\times10^6$, $5\times10^6$, and $1.4\times10^7$ source electrons are simulated for the lead and HD concrete stacking, and $2\times10^6$, $1.2\times10^7$, and $2.4\times10^7$ source electrons are simulated for the iron and HD concrete stacking, respectively. For the lead and borated polyethylene stacking, $5.4\times10^6$ source electrons are simulated at a total thickness of 3 m.

backscatter radiation and facilitates the comparison between the three-layer and five-layer stacking methods. For the following four layers, each layer has a thickness of $L_1/2$ and $L_2/2$ for low-Z and high-Z layer, respectively. For the second five-layer design, as illustrated on the right side of Fig. 1(b), the first layer always has a thickness of one fifth of the total shielding thickness. This choice ensures a similar magnitude of backscatter when the high-Z layer thickness is varied. For the following layers, the partition of different layers is the same as in the first five-layer design.

Three tissue dose monitors are placed 30 cm away from the beam dump, 1 m above the floor, and have an inter-spacing of 20 cm (D1, D2 and D3 in Fig. 1)(a)). Each dose monitor has dimensions of 40 cm (width) × 20 cm (thickness) × 60 cm (height). The energy deposition, ambient dose equivalent, and particle spectra are extracted from these dose monitors for the analysis. The ambient dose equivalent is determined based on the conversion factors from Refs. International Commission on Radiological Protection (1996) and Pelliccioni (2000). For an actual lab setting, there is usually a laboratory wall that separates personnel from the accelerator room and further reduces the dose, but here we are concerned mostly about the variation of the dose with different shielding configurations. The lab walls and roof are not included in the simulations to simplify the studied problem, but the interactions of radiation with these objects will have an impact on the distribution of the energy deposition and should be included in the simulation of an actual facility. The compositions of major materials used in the simulation are listed in Table 1. The HD concrete can have a wide range of densities and elemental compositions. For this analysis we selected a density of 2.4 g/cm$^3$ with 7.4% carbon, 46.0% oxygen, 11.1% iron, and 29.5% calcium (all weight percentages).

**Table 1**
Material compositions used in the FLUKA and Geant4 simulations. The HD concrete, ICRP soft tissue, and boron-loaded polyethylene have a density of 2.4 g/cm$^3$, 1.0 g/cm$^3$, and 0.969 g/cm$^3$, respectively.

| HD concrete | | ICRP soft tissue | | Boron-loaded polyethylene | |
|---|---|---|---|---|---|
| Atomic number | wt. % | Atomic number | wt. % | Atomic number | wt. % |
| 1 | 0.58 | 1 | 10.4472 | 1 | 13.45 |
| 6 | 7.42 | 6 | 23.2190 | 5 | 5.00 |
| 8 | 46.03 | 7 | 2.4880 | 6 | 81.55 |
| 11 | 0.04 | 8 | 63.0238 | | |
| 12 | 1.44 | 11 | 0.1130 | | |
| 13 | 0.55 | 12 | 0.0130 | | |
| 14 | 3.09 | 15 | 0.1330 | | |
| 16 | 0.18 | 16 | 0.1990 | | |
| 19 | 0.10 | 17 | 0.1340 | | |
| 20 | 29.47 | 19 | 0.1990 | | |
| 26 | 11.1 | 20 | 0.0230 | | |
| | | 26 | 0.0050 | | |
| | | 30 | 0.0030 | | |

The PRECISIOn physics package is used in the FLUKA simulation. In addition, the photon–nucleus interactions are included by the PHOTONUC card and the muon pair production is included by the MUMUPAIR card. For the beam dump materials, the electron and photon production cuts are set to 500 keV and 100 keV, respectively. In the tissue, both cuts are set to 100 keV. Similar geometry is also modeled in Geant4 (version 10.06.p01) for comparison (Agostinelli et al., 2003), as shown in Fig. 1(c). The QGSP_BIC_HP physics package is used in Geant4 with particle production cuts in similar range.

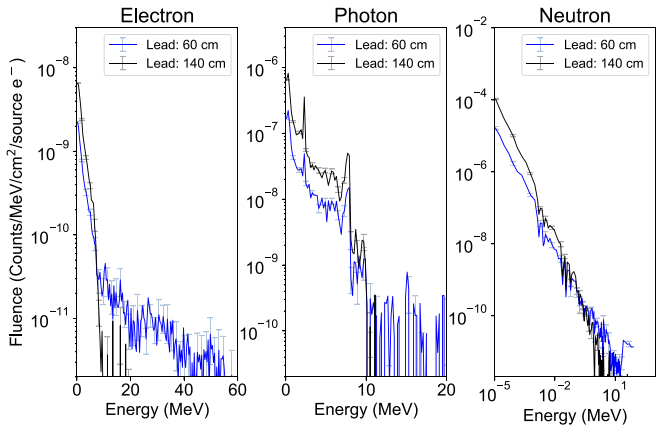


**Fig. 3.** Track-length fluence of electrons, photons, and neutrons on the central dose monitor with the lead and HD concrete stacking at a total thickness of 2 m with an electron energy of 10 GeV.

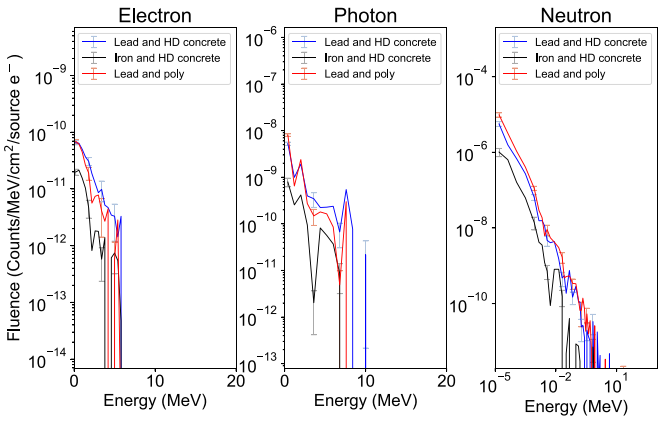


**Fig. 4.** Track-length fluence of electrons, photons, and neutrons on the central dose monitor for a total shielding thickness of 3 m at 10 GeV. The fluences here correspond to the configuration that gives the minimum dose for each stacking method. The high-Z layer thickness is 120 cm, 220 cm, and 180 cm for the lead and HD concrete, iron and HD concrete, and lead and polyethylene stacking, respectively.

## 3. Results and discussion

### 3.1. Various material combinations at 10 GeV

Fig. 2 shows the impact of high-Z layer thickness ($L_2$ in Fig. 1(b)) on the maximum dose equivalent from the three dose monitors for a total shielding thickness of 2 m, 3 m, and 4 m at 10 GeV. Different shielding thicknesses are simulated to accommodate a range beam parameters, including the pulse repetition rate, the beam charge per shot, and the thickness of other radiation barriers. At a total thickness of 2 m, the minimum dose corresponds to a lead thickness of ~80–100 cm for the case of lead. In iron and HD concrete stacking, the dose keeps decreasing with the increase of iron thickness, but at a reduced rate as the iron thickness approaches the total thickness. Below 40 cm of thickness, iron is not sufficient to reduce the flux of high-energy photons and electrons, but with the increase of iron thickness, this material combination (iron and HD concrete) is in fact superior to lead and HD concrete, producing a dose that is ~ 6.9× lower. At the total thickness of 2 m, the highest dose is deposited in the central dose monitor that is aligned with the beam.

At a thickness of 3 m, similar trends are observed, where the lowest dose corresponds to a thickness of 120 cm for lead and 220 cm for iron. The lowest dose with iron is about 7.4× lower than that of lead. When the lead and concrete stacking is changed to lead and borated polyethylene, the lowest dose stays approximately the same, but it requires an even thicker layer of lead. Although carbon and hydrogen are very efficient in slowing down neutrons and B-10 has a high cross-section of thermal neutron capture, surprisingly, the overall response to 10-GeV electrons does not exhibit significant improvement. At the total thickness of 3 m, with the increase of the high-Z layer thickness, the highest dose is now recorded by the side dose monitors because of increased scattering. For example, for iron and concrete stacking, this starts to occur from an iron thickness of 160 cm.

At a total thickness of 4 m, the difference between the two stacking configurations becomes smaller, with the iron configuration being only 2.6× lower. This is because 4 m is enough to block most of the radiation and only interaction cascades that produce highly penetrating radiation can reach the dose monitors. For the same reason, the statistical fluctuation of the dose is larger than the previous two thicknesses although more source electrons are simulated.

An notable trend can be seen for lead and HD concrete (see Fig. 2(a)), where the dose increases with increasing thickness after reaching a minimum. Fig. 3 shows the energy spectra at the central dose monitor for two different lead thicknesses. A thicker layer of lead results in a higher fluence at low electron energy but a lower

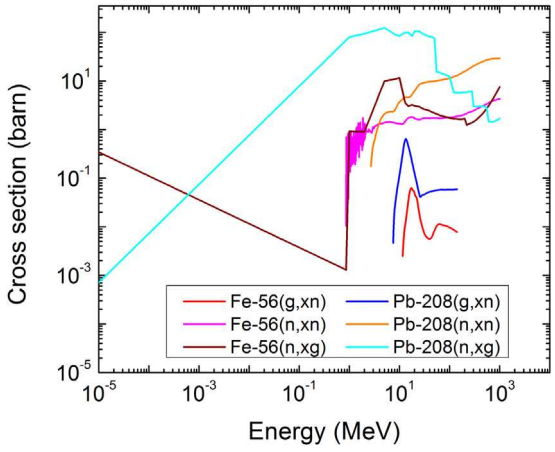


**Fig. 5.** Cross-sections for neutron and gamma production from $^{56}$Fe and $^{208}$Pb. The (g,xn) cross-sections are taken from the JENDL/PD-2004 library, while the (n,xn) and (n,xg) cross-sections are taken from the ENDF/HE-VI library.

fluence at high energy. For photons and neutrons, the same behavior is observed. This can be explained by the fact that a thicker lead layer allows fewer high-energy electrons and photons to penetrate the beam dump, but on the other hand, interactions within lead can produce neutrons and low-energy electrons and photons. Intuitively, due to the higher attenuation capability of lead for high-energy photons, one might expect a softer electron and photon spectrum. However, lead can also generate radiation from photonuclear reactions and neutron-induced reactions, which leads to the spectral shapes shown in Fig. 3. Similar behavior is also observed for a total thickness of 3 m. However, at a thickness of 4 m, it is hard to compare the spectra due to the limited particle statistics at the dose monitors.

The fluences of electrons, photons, and neutrons for the optimal stacking configuration at a total thickness of 3 m are shown in Fig. 4. Several conclusions can be drawn from this optimization. First, the use of iron reduces the fluence for all three types of particles when compared to lead. This can be explained by the neutron and gamma cross-sections shown in Fig. 5 where cross-sections of $^{56}$Fe and $^{208}$Pb, the dominant isotope in iron and lead, are compared. The natural iron and lead is made of 91.8% $^{56}$Fe and 52.4% $^{208}$Pb, respectively. The total neutron production cross-section induced by photons, (g,xn), is one order of magnitude higher in $^{208}$Pb than in $^{56}$Fe. The total gamma production cross-section induced by neutrons, (n,xg), is also

**Table 2**
Comparison of the absorbed dose between FLUKA and Geant4 simulations at a total shielding thickness of 1 m. At least $8 \times 10^5$ source electrons are used in both simulations.

| Condition: 30 cm HD concrete + 40 cm lead + 30 cm HD concrete | | |
|---|---|---|
| | Central dose monitor (μGy/nC) | Side dose monitor (μGy/nC) |
| FLUKA | 0.82 ± 0.02 | 0.36 ± 0.08 |
| Geant4 | 0.88 ± 0.08 | 0.51 ± 0.03 |
| Difference (%) | 12.2 | 24.8 |

much higher in $^{208}$Pb than $^{56}$Fe over most of the energy range. For (n,xn) reactions, $^{56}$Fe has a lower threshold of 0.86 MeV, but the cross-section of $^{208}$Pb becomes higher when the neutron energy is above 3.9 MeV. Based on these cross-section data, it can be seen that it is much easier to convert neutrons to gamma rays and convert high-energy photons to neutrons within lead. When comparing the spectra between HD concrete and borated polyethylene, the magnitude of fluence and the overall shape of the spectra look very similar. The use of borated polyethylene does not seem to bring additional benefit in these specific conditions. We also tested these material combinations at a total shielding thickness of 1 m and, interestingly, the combination of borated polyethylene and lead can actually reduce the dose to the level ~11× lower than that for a combination of HD concrete and lead. Therefore, the relative shielding performance of materials is thickness-dependent. Since a total thickness of 1 m is relatively thin for electron beam shielding, the attenuation and conversion of particles are different from that at a total thickness of 3 m, which results in different shielding effectiveness.

The absorbed doses calculated by FLUKA and Geant4 are compared for the concrete and lead stacking and are presented in Table 2. The dose monitors show a maximum dose difference of ~25%, which is expected due to the statistical fluctuations and difference in the implementation of the cross-sections and physics models in the two Monte Carlo codes. For example, it has been noted that the photoneutron cross-sections used in those two codes can be different by ~12% at a photon energy of ~13.5 MeV in lead (Quintieri et al., 2017). For 510-MeV electrons incident on tungsten target, the neutron production rate can differ by 70% and the proton production rate also differs by 22% (Quintieri et al., 2017). In Geant4, the photonuclear cross-sections are available for 50 nuclei; 14 of them are used for parameterization to describe the cross-sections in five different energy regions (the Giant Dipole Resonance region, the "quasi-deuteron" region, the Delta region, the Roper resonance, and the Reggeon–Pomeron region) (Agostinelli et al., 2003). In FLUKA, the photonuclear cross-sections of 190 nuclei are available and four different energy regions are used to parameterize the cross-sections (Quintieri et al., 2017; Fasso et al., 1994). Considering the fact that different nuclear data and models are used, the results on energy deposition are consistent between the two codes. In addition, the electron beam simulation in FLUKA has shown good agreement with experimental data (Battistoni et al., 2007) and cross-sections have also been benchmarked with neutron spectroscopy experiments and activation measurements (Fassò et al., 2005). It is, however, necessary to use a certain safety margin for the shielding design to account for the differences between the actual and simulated dose. By examining each interaction in Geant4, it is found that some rare interactions can deposit a significant amount of energy inside the dose monitor. In one instance, a 1.7 GeV neutron is produced and interacts with $^{16}$O in air close to the dose monitor. This reaction produces multiple protons, neutrons, pions, and deuterons with kinetic energies up to several hundred MeVs, and such one event deposits more than 500 MeV in the dose monitor. Such rare events with large energy deposition can also create large statistical fluctuations for the simulated dose.

### 3.2. Comparison of the three-layer and five-layer stacking

The results of the three-layer and five-layer stacking methods are compared in Fig. 6. The stacking geometry has been discussed earlier in Fig. 1(b) and the Methods section. When each layer is thinner, the high-energy photons/neutrons generated from the low-Z/high-Z layer can be effectively slowed down by the next high-Z/low-Z layer, respectively, and the decrease of their energy can potentially help decrease the dose. For the lead and HD concrete stacking, the first five-layer stacking method can reach a dose that is 22%–41% lower in the 80–160 cm range. The dose distributions projected in the horizontal plane are shown in Fig. 7. It can be seen from Fig. 7(c) and (d) that the two configurations produce similar levels of backscatter, but the dose in front of the beam dump and at the two sides are apparently higher for the three-layer configuration. Inside the beam dump, the boundary between different layers can also be observed from Fig. 7(a) and (b) based on the dose level. The results here show that it is possible to reduce the dose by simply changing the stacking sequence of different layers. For the second five-layer stacking method, the dose is 19% to 52% lower than the three-layer stacking. However, the backscatter is more pronounced for this stacking method because the first layer of HD concrete has a thickness of 60 cm instead of 80 cm, which leads to a higher transmission rate of backscattering from the second layer of lead. For the case of 52% lower dose, which corresponds to a lead thickness of 80 cm, the higher extent of backscatter is clearly observed by obtaining similar dose maps to Fig. 7. Comparing the three different stacking methods, we see that the variation of the dose with the lead thickness shows a similar behavior, where the dose increases with further increases of thickness once it reaches a minimum. The different stacking methods can lead to different spatial dose distributions both at the front and at the back side, and the optimal choice of the stacking design depends on the overall shielding design and the shielding goals for the accelerator facility.

In contrast to the results from lead and concrete, for the iron and HD concrete stacking, the dose from the five-layer configuration is on average ~35% higher (see Fig. 6). As shown in Fig. 8, the magnitude of backscatter is similar but only the front dose becomes higher, which is reflected by an overall higher dose in the $y < -600$ cm region. The inferior performance with the five-layer stacking is due to the fact that iron does not generate as many neutrons and photons as lead. In addition, the difference in neutron attenuation between iron and low-Z materials is small because iron has a relatively high neutron inelastic cross-section that can slow down neutrons, especially below 3 MeV (Herman et al., 2018). Thus, dividing the thickness into more layers is not beneficial for this material combination. For the lead and borated polyethylene stacking, the five-layer stacking can reach a dose that is 30%–42% lower (see Fig. 6(c)). Based on these results, it is concluded that using a greater number of interleaved layers is effective in reducing the dose when lead is used, but is not beneficial with the use of iron. It has been previously shown that, under certain conditions, the iron and HD concrete stacking can reach a dose that is ~ 7× lower than lead, so the improvement brought by the multilayer stacking seems not to be comparable to the improvement brought by the change of materials. On the other hand, iron has the performance similar to lead when the high-Z layer thickness is $\lesssim$40% of the total thickness. If the thickness of the high-Z layer is limited or there is lead readily available, using interleaved layers of lead and concrete is still a suitable choice for electron shielding.

### 3.3. Optimal configuration at 1 GeV and 40 GeV

The variation of the dose at 1 GeV and 40 GeV is presented in Fig. 9. At 1 GeV and a total thickness of 2 m, similar behavior is observed for the lead and concrete stacking, where the dose starts to increase with increasing thickness once it reaches a minimum. The dose at 70 cm seems not to exactly follow the overall trend. However, $4 \times 10^7$ source

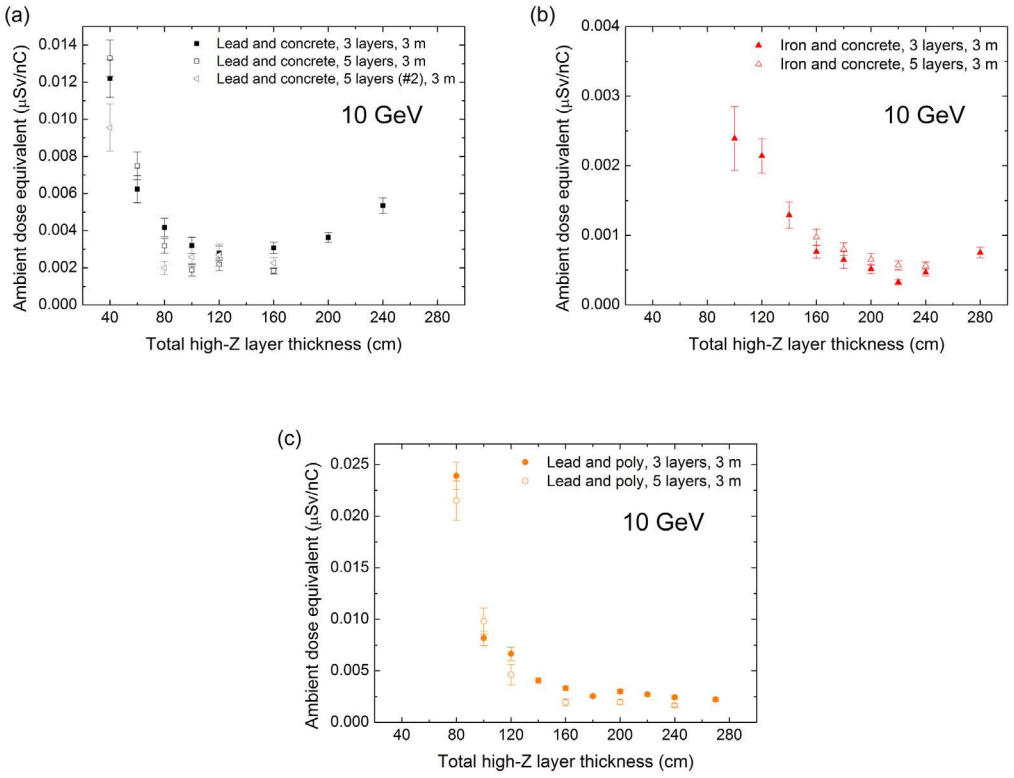


**Fig. 6.** Comparison of the three-layer and five-layer stacking configurations at an electron energy of 10 GeV at a total shielding thickness of 3 m. The stacking materials consist of (a) lead and HD concrete, (b) iron and HD concrete, and (c) lead and 5 wt.% boron-loaded polyethylene.

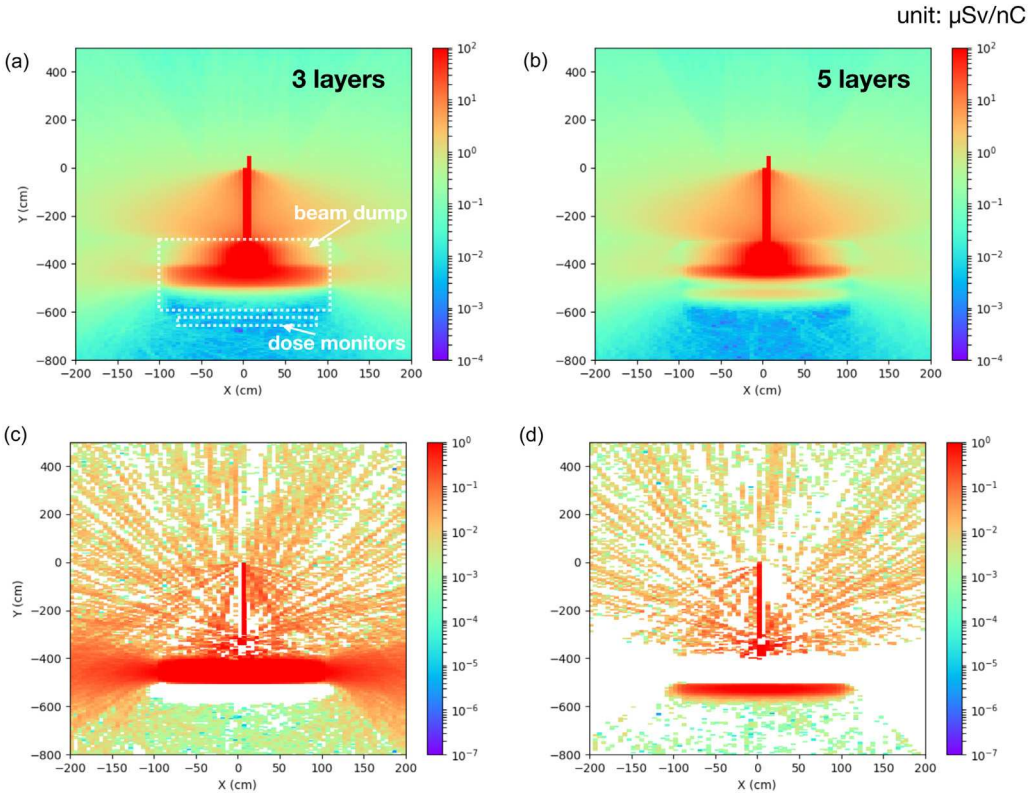


**Fig. 7.** Comparison of the ambient dose equivalent between the (a) three-layer and (b) five-layer stacking configuration with the HD concrete and lead stacking at a lead thickness of 80 cm. The dose maps are projected in the $z$-direction perpendicular to the floor. The electron beam is in the $-y$ direction and the beam dump is located between $y = -300$ cm and $y = -600$ cm. The difference (subtraction of the five-layer dose from the three-layer dose) between the two configurations is shown in (c) and (d). Since only positive values can be shown in logarithmic scale, if the difference is positive, the dose is shown in (c); if the difference is negative, the sign is inverted and shown in (d).

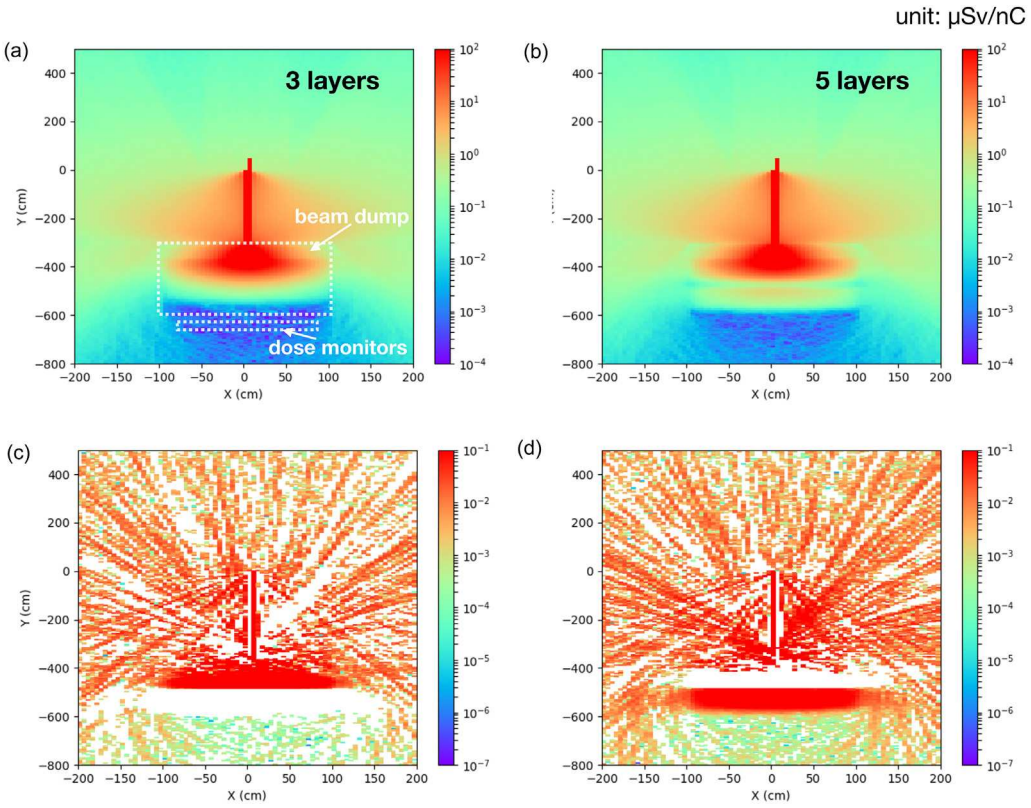


**Fig. 8.** Comparison of the ambient dose equivalent between the (a) three-layer and (b) five-layer stacking configuration with the HD concrete and iron stacking at an iron thickness of 160 cm. The dose maps are projected in the $z$-direction perpendicular to the floor. The electron beam is in the $-y$ direction and the beam dump is located between $y = -300$ cm and $y = -600$ cm. The difference (subtraction of the five-layer dose from the three-layer dose) between the two configurations is shown in (c) and (d). Since only positive values can be shown in logarithmic scale, if the difference is positive, the dose is shown in (c); if the difference is negative, the sign is inverted and shown in (d).

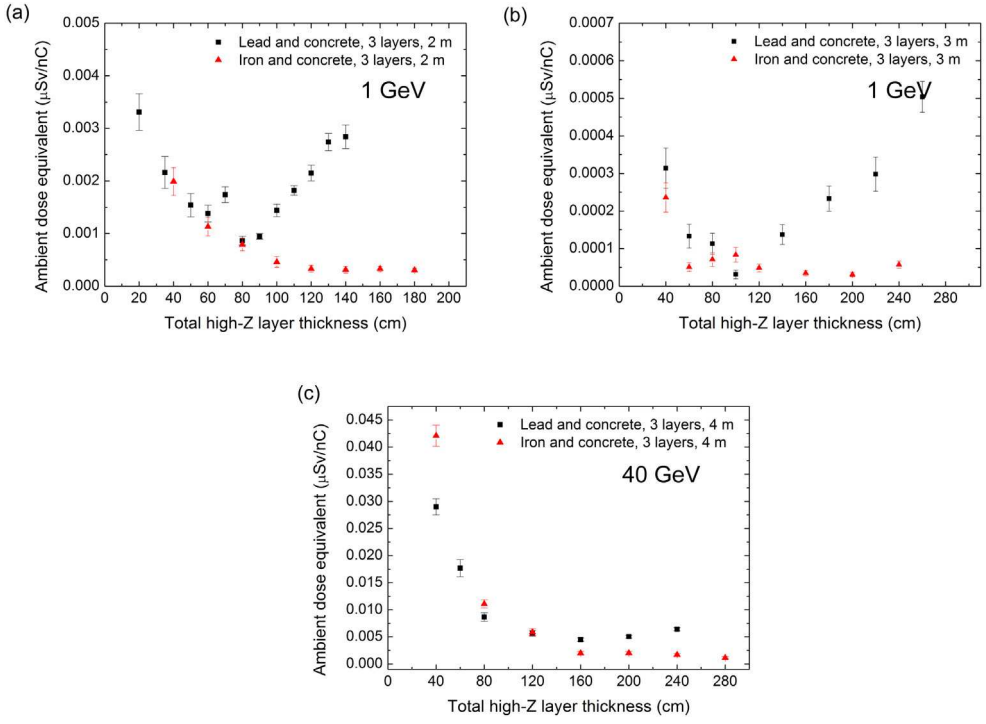


**Fig. 9.** Variation of the ambient dose equivalent with the high-Z layer thickness for different shielding configurations for an electron energy of (a,b) 1 GeV and (c) 40 GeV. A total thickness of (a) 2 m and (b) 3 m is simulated at 1 GeV.

electrons have been simulated for this condition, which is twice as many as the other conditions and gives a standard deviation of 8.6% based on the FLUKA uncertainty evaluation. The higher dose could be induced by some rare interactions with large energy deposition within

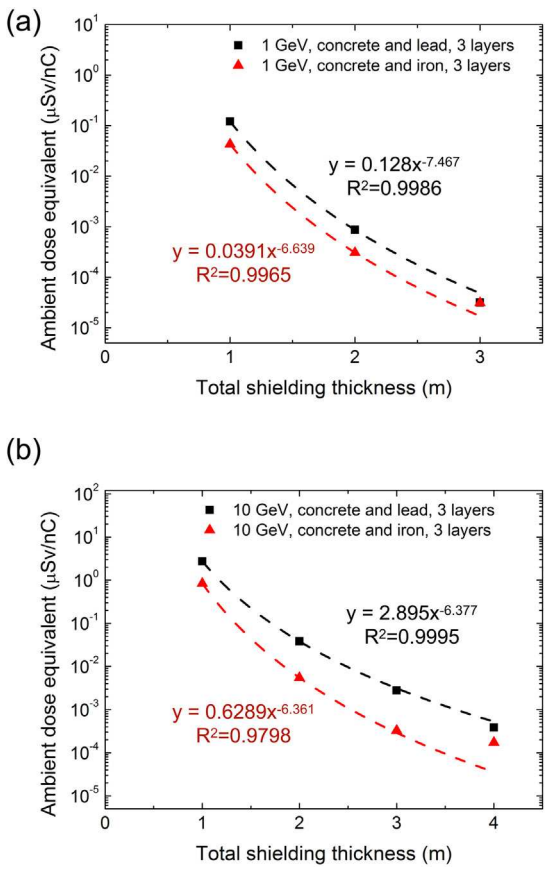


**Fig. 10.** Variation of the minimum dose equivalent with the total shielding thickness for (a) 1-GeV and (b) 10-GeV electrons.

the scoring volume. For the iron and concrete stacking, starting from 120 cm, the dose equivalent converges to $3.2 \times 10^{-4}$ μSv/nC, which is 2.7× lower than the minimum dose from lead and concrete. At 1 GeV and a total thickness of 3 m, a larger statistical fluctuation is observed because the beam dump is less penetrating. Interestingly, at this thickness, the optimal dose from the two configurations is approximately the same. This is consistent with the finding from the case of 10-GeV electrons and 4-m thickness in the sense that, when the shielding is thick relative to the electron energy, the difference between the two configurations is smaller. By examining the spectra of different types of radiation and comparing the energy deposition and dose equivalent, it is found that neutrons are a major contributor to the dose equivalent. Thus, absorbing neutrons and reducing the production of secondary neutrons is important for the shielding of electrons at this energy.

At an electron energy of 40 GeV and a total thickness of 4 m, a lead thickness of 160 cm gives a minimum dose of $4.5\times10^{-3}$ μSv/nC. For the iron and HD concrete stacking, the minimum dose of $1.1\times10^{-3}$ μSv/nC is obtained at an iron thickness of 280 cm. With the lead and HD concrete stacking, the fraction of the dose equivalent from neutrons varies from 41% to 61%, but for iron, with the increase of its thickness, this fraction changes from 48% to 16%, showing the importance of reducing the neutron flux for reducing the dose. For such high electron energy, muon production becomes non-negligible as well. For an electron accelerator that operates at this high energy, when the repetition rate or the beam power is high, a thicker shielding is potentially needed. Due to the limitation on computational resources, a wide range of shielding thicknesses is not simulated here for such parametric study.

Fig. 10 shows the minimum dose as a function of the total shielding thickness at 1 GeV and 10 GeV. Due to the complexity of the electron interactions, the obtained power law fits should only be applied for the simulated range of parameters. The fits describe well the obtained trends except for 10-GeV electrons with concrete and iron stacking, for which the last data point at 4 m starts to level off and distort the trendline. The maximum difference between the fits and the data points at 1 GeV is 16% and 28% for the lead and iron configuration, respectively, and this difference is 9.7% and 77% for lead and iron at 10 GeV.

## 4. Conclusions

We simulated several material structures to determine the optimal design of the electron beam dump for GeV-class laser-driven electron accelerators. An electron energy of 1, 10, and 40 GeV was simulated with the FLUKA code and a comparison with Geant4 was performed at 10 GeV, showing relatively good consistency with ~20% difference in the absorbed dose. With FLUKA simulations, it is found that the iron and high-density concrete stacking and the lead and high-density concrete stacking have similar performance when the iron or lead thickness is $\lesssim$40% of the total beam dump thickness. When the high-Z layer thickness is $\gtrsim$40%, the use of iron can reduce the radiation dose to a level several times lower than that of lead depending on the total shielding thickness and the electron energy. This is due to the fact that the cross-sections for neutron and photon production in iron are smaller than lead. The difference in performance between the aforementioned two configurations tends to be smaller when the total shielding thickness is thicker. The lowest dose at 1, 10, and 40 GeV corresponds to the iron and high-density concrete stacking with an iron thickness close to the total shielding thickness. Reasonably good shielding performance can also be achieved with a lower fraction of iron or with the use of lead and high-density concrete stacking. No significant change in the dose equivalent is found when replacing the high-density concrete with borated polyethylene in the combination of lead and concrete at a shielding thickness of 3 m at 10 GeV. However, this replacement leads to a lower dose when the total shielding thickness is 1 m, showing dependence of shielding response on beam dump thickness. When the three-layer stacking method is changed to five-layer stacking, it can lead to a ~20%–40% reduction in dose with the use of lead, but the five-layer stacking results in a higher dose in the case of iron. Based on this study, we show that the performance of the beam dump has a large dependence on the materials used, the electron energy, and the beam dump configuration. These results provide the general guidance for choosing the efficient shielding methods for high-energy electron accelerators, which will particularly benefit the compact laser-driven accelerators.

## CRediT authorship contribution statement

**T. Shi:** Writing - original draft, Methodology, Simulation, Formal analysis. **D. Sun:** Simulation, Formal analysis. **I. Jovanovic:** Writing, Methodology, Supervision. **G. Kalinchenko:** Supervision. **K. Krushelnick:** Supervision. **C.C. Kuranz:** Supervision. **A. Maksimchuk:** Methodolody, Supervision. **J. Nees:** Methodology, Supervision. **A.G.R. Thomas:** Supervision. **L. Willingale:** Supervision.

## Declaration of competing interest

The authors declare that they have no known competing financial interests or personal relationships that could have appeared to influence the work reported in this paper.

## Acknowledgments

This work was supported by the National Science Foundation, United States through grant PHY-1935950 and in part through computational resources and services provided by Advanced Research Computing at the University of Michigan, United States.

## References


Agostinelli, S., Allison, J., Amako, K.a., Apostolakis, J., Araujo, H., Arce, P., Asai, M., Axen, D., Banerjee, S., Barrand, G.., et al., 2003. GEANT4—a simulation toolkit. Nucl. Instrum. Methods Phys. Res. A 506 (3), 250–303.

Battistoni, G., Cerutti, F., Fasso, A., Ferrari, A., Muraro, S., Ranft, J., Roesler, S., Sala, P., 2007. The FLUKA code: Description and benchmarking. In: AIP Conference Proceedings, Vol. 896. American Institute of Physics, pp. 31–49.

Englbrecht, F.S., Döpp, A., Hartmann, J., Lindner, F.H., L, G.M., Wirth, H.-F., Thirolf, P.G., Karsch, S., Schreiber, J., Parodi, K., Dedes, G., 2020. Radiation protection modelling for 2.5 petawatt-laser production of ultrashort x-ray, proton and ion bunches: Monte Carlo model of the munich CALA facility. J. Radiol. Prot. 40 (4), 1048–1073.

Esarey, E., Schroeder, C.B., Leemans, W.P., 2009. Physics of laser-driven plasma-based electron accelerators. Rev. Modern Phys. 81, 1229–1285.

Fassò, A., Ferrari, A., Sala, P.R., 2005. Photonuclear reactions in FLUKA: cross sections and interaction models. In: AIP Conference Proceedings, Vol. 769. American Institute of Physics, pp. 1303–1306.

Fasso, A., et al., 1994. Proceedings of the Eighth Int. Conf on Radiation Shielding.

Faure, J., Glinec, Y., Pukhov, A., Kiselev, S., Gordienko, S., Lefebvre, E., Rousseau, J.P., Burgy, F., Malka, V., 2004. A laser–plasma accelerator producing monoenergetic electron beams. Nature 431 (7008), 541–544.

Ferrari, A., Amato, E., Margarone, D., Cowan, T., Korn, G., 2013. Radiation field characterization and shielding studies for the ELI beamlines facility. Appl. Surf. Sci. 272, 138–144.

Geddes, C.G.R., Toth, C., van Tilborg, J., Esarey, E., Schroeder, C.B., Bruhwiler, D., Nieter, C., Cary, J., Leemans, W.P., 2004. High-quality electron beams from a laser wakefield accelerator using plasma-channel guiding. Nature 431 (7008), 538–541.

Gonsalves, A., Nakamura, K., Daniels, J., Benedetti, C., Pieronek, C., De Raadt, T., Steinke, S., Bin, J., Bulanov, S., Van Tilborg, J., et al., 2019. Petawatt laser guiding and electron beam acceleration to 8 gev in a laser-heated capillary discharge waveguide. Phys. Rev. Lett. 122 (8), 084801.

Herman, M., Trkov, A., Capote, R., Nobre, G., Brown, D., Arcilla, R., Danon, Y., Plompen, A., Mughabghab, S., Jing, Q., et al., 2018. Evaluation of neutron reactions on iron isotopes for CIELO and ENDF/B-VIII. 0. Nucl. Data Sheets 148, 214–253.

International Commission on Radiological Protection, 1996. ICRP Publication 74: Conversion Coefficients for Use in Radiological Protection Against External Radiation, Vol. 23. Elsevier Health Sciences.

Leemans, W., Gonsalves, A., Mao, H.-S., Nakamura, K., Benedetti, C., Schroeder, C., Tóth, C., Daniels, J., Mittelberger, D., Bulanov, S., et al., 2014. Multi-gev electron beams from capillary-discharge-guided subpetawatt laser pulses in the self-trapping regime. Phys. Rev. Lett. 113 (24), 245002.

Maksimchuk, A., Reed, S., Bulanov, S.S., Chvykov, V., Kalintchenko, G., Matsuoka, T., McGuffey, C., Mourou, G., Naumova, N., Nees, J., et al., 2008. Studies of laser wakefield structures and electron acceleration in underdense plasmas. Phys. Plasmas 15 (5), 056703.

Maksimchuk, A., Reed, S., Naumova, N., Chvykov, V., Hou, B., Kalintchenko, G., Matsuoka, T., Nees, J., Rousseau, P., Mourou, G., et al., 2007. Energy scaling of quasi-monoenergetic electron beams from laser wakefields driven by 40-TW ultra-short pulses. Appl. Phys. B 89 (2–3), 201–207.

Mangles, S.P.D., Murphy, C.D., Najmudin, Z., Thomas, A.G.R., Collier, J.L., Dangor, A.E., Divall, E.J., Foster, P.S., Gallacher, J.G., Hooker, C.J., Jaroszynski, D.A., Langley, A.J., Mori, W.B., Norreys, P.A., Tsung, F.S., Viskup, R., Walton, B.R., Krushelnick, K., 2004. Monoenergetic beams of relativistic electrons from intense laser–plasma interactions. Nature 431 (7008), 535–538.

Mao, X., Leitner, M.S., Vollaire, J., 2011. Facility for Advanced Accelerator Experimental Tests (FACET) at SLAC and its Radiological Considerations. Tech. Rep., SLAC National Accelerator Laboratory, Menlo Park, CA (United States).

Nees, J., Maksimchuk, A., Kalinchenko, G., Hou, B., Ma, Y., Campbell, P., McKelvey, A., Willingale, L., Jovanovic, I., Kuranz, C., Thomas, A., Krushelnick, K., 2020. ZEUS: A national science foundation mid-scale facility for laser-driven science in the QED regime. In: Conference on Lasers and Electro-Optics. Optical Society of America, p. JW2B.9.

OECD, 2015. Shielding Aspects of Accelerators, Targets and Irradiation Facilities-SATIF-12: Workshop Proceedings, Batavia, Illinois, United States, 28-30 April 2014. OECD Publishing.

Pelliccioni, M., 2000. Overview of fluence-to-effective dose and fluence-to-ambient dose equivalent conversion coefficients for high energy radiation calculated using the FLUKA code. Radiat. Prot. Dosim. 88 (4), 279–297.

Quintieri, L., Pia, M.G., Augelli, M., Saracco, P., Capogni, M., Guarnieri, G., 2017. Quantification of the validity of simulations based on geant4 and FLUKA for photonuclear interactions in the high energy range. In: EPJ Web of Conferences, Vol. 153. EDP Sciences, p. 06023.

Rokni, S., 1996. Radiation protection system for the final focus test beam at SLAC (revised). Health Phys. 71 (SLAC-PUB-6784).

Rokni, S.H., Cossairt, J.D., Liu, J.C., et al., 2007. Radiation Shielding at High-Energy Electron and Proton Accelerators. Tech. Rep., Stanford Linear Accelerator Center (SLAC).

Stevenson, G.R., 2001. Induced activity in accelerator structures, air and water. Radiat. Prot. Dosim. 96 (4), 373–379.

Vylet, V., Liu, J.C., 2001. Radiation protection at high energy electron accelerators. Radiat. Prot. Dosim. 96 (4), 333–343.